LAWRENCE
LIVERMORE
NATIONAL
LABORATORY

LLNL-JRNL-407151

Nonlinear Rayleigh-Taylor instabilities in fast z-pinches

A. R. Miles

September 22, 2008

Physics of Plasmas

Disclaimer

Nonlinear Rayleigh-Taylor instabilities in fast z-pinches

Aaron R. Miles

Lawrence Livermore National Laboratory, Livermore, California 94550

A simplified analytic model is presented to describe the implosion of a plasma column by an azimuthal magnetic field of sufficient magnitude to drive a strong shock wave into the plasma. This model is employed together with buoyancy-drag-based models of nonlinear single-mode and turbulent multimode Rayleigh-Taylor (RT) growth to investigate the mixing process in such fast z-pinches. These models give predictions that characterize limitations the instability can impose on the implosion in terms of maximum convergence ratios (CR) attainable for an axially coherent pinch. Both the implosion and instability models are validated with results from high-resolution numerical simulations.

I. INTRODUCTION

Rayleigh-Taylor (RT) instabilities[1,2] are ubiquitous in nature, and z-pinches offer an important platform for their study. In a z-pinch, the driving magnetic field plays the role of the lighter fluid accelerating the plasma cylinder, which acts as the heavier fluid.[3-5] The driving magnetic pressure and the plasma thermal pressures are given, respectively, by

$$P_B = \frac{5}{\pi}\left(\frac{I_{MA}}{R_{cm}}\right)^2 kbar \qquad (1)$$

$$P_{th} = 0.0227 \rho_{mg/cc} \frac{(1+Z)}{A} \frac{T}{T_0} kbar, \qquad (2)$$

where I_{MA} is the driving current in MA, R_{cm} is the initial radius of the plasma cylinder in cm, $\rho_{mg/cc}$ is the plasma mass density in mg/cm^3, Z, A, and T are its charge state, atomic weight, and temperature, and $T_0 = 273.15$ K.

A fast z-pinch is the implosion of a plasma cylinder behind a cylindrically convergent shock wave driven by a high-current discharge. If the condition $P_B >> P_{th}$ is satisfied, then the Mach number of the implosion shock will be high.

In any such magnetic implosion, the total pressure (the sum of magnetic and thermal pressures) and density gradients have opposite signs at the plasma-vacuum interface. Consequently, the interface is RT unstable. Instabilities can allow for local plasma compression beyond the radius at which hydro-magnetic equilibrium is established after first bounce, but also limit the maximum convergence ratio (CR) attainable for an axially coherent pinch.[6]

In this paper, we employ a simplified analytic z-pinch model together with nonlinear and turbulent RT growth models based on the buoyancy-drag picture[7-10] to investigate the mixing process in fast z-pinches. These models allow us to characterize limitations that the instability can impose on the implosion in terms of maximum CR for an axially coherent pinch. The implosion model is compared to 1D implosion simulations, and the instability model is compared and calibrated with 2D high-resolution numerical simulations.

II. IMPLOSION MODEL

The basic z-pinch geometry is shown in Fig. 1a. We assume an infinitely long plasma column with initial radius R_0. An electrical current of arbitrary time-dependence is applied to the outer surface of the plasma column, resulting in a time-dependent implosion velocity $v(t) = dR(t)/dt$. If the time-dependent current is parameterized by $I(t) = I_0\beta(t)$, where I_0 is a characteristic dimensional current and the time-dependence is contained in the dimensionless function $\beta(t)$, then the magnetic pressure can be written as

$$P_B(t) = \frac{1}{2}\rho_0 u_0^2 \left(\frac{R_0}{R(t)}\right)^2 \beta^2(t), \tag{3}$$

where ρ_0 is the initial pre-shock plasma density and the characteristic speed u_0 is given by $u_0 \equiv I_0 / \left(R_0 c\sqrt{\pi\rho_0}\right)$ in cgs units.

Within the fast z-pinch model, the only limitation on the driving current is that its magnitude is sufficiently high that a strong shock wave is driven into the plasma. The strong-shock limit allows for a very simple analytic model of the implosion based on three main statements. First, pressure balance between the shocked plasma and B-field gives

$$P_B = P_{th}^*, \tag{4}$$

where the asterisk denotes a post-shock quantity. Second, we use equapartition of energy behind a strong shock to relate the thermal and dynamic pressures:

$$\frac{1}{\gamma - 1} P_{i,s}^* = \frac{1}{2}\rho_s^* u_s^2, \tag{5a}$$

where P_i is the ion pressure the subscript s denotes values just behind the shock front. Since we will always work in the lab frame where there is no flow ahead of the shock,

asterisks will be omitted on velocities. Thus u_s is the fluid velocity just behind the shock front.

Finally, we need to identify a relationship between pressure, density, and velocity just behind the shock front with the same quantities at the interface. If we neglect gradients in the shocked plasma and include a factor to account for cylindrical convergence, then the last two model components are expressed as

$$\frac{1}{\gamma-1}P_{th}^{*}=\frac{1}{2}\rho_{s}^{*}\frac{R_0}{R}v^2, \tag{5b}$$

where v is the plasma-vacuum interface velocity.

As we shall see, the model based on Eqs. 3, 4, and 5b does a remarkable job of capturing the 1D pinch trajectory for a variety of current forms even when there are significant density, pressure, and velocity gradients in the shocked plasma. Consequently, we will make as our third model component the as yet unsubstantiated assumption that

$$P_{th}^{*}=P_{i,s}^{*}\frac{R_0}{R}\left(\frac{v}{u_s}\right)^2, \tag{6}$$

in order to recover Eq. (5b) from (5a). For an isothermal plasma, there is then a corresponding relationship for the plasma density, which grows due to the initial strong shock, cylindrical convergence, and radial convergence when the implosion speed at the interface (v) exceeds the implosion speed just behind the shock. The extent to which Eq. (6) is a reasonable assertion will be checked later by comparing with 1D numerical simulations.

We define dimensionless radius, velocity, and acceleration variables $\xi \equiv R/R_0$, $\tau \equiv t/t_0$, and $t_0 \equiv \frac{2}{3}\sqrt{\gamma+1}R_0/u_0$, in terms of which Eq. (4) becomes a first-order differential equation for the pinch radius:

$$\xi^{1/2}\frac{d\xi}{d\tau} = -\frac{2}{3}\beta(\tau). \tag{7a}$$

This can be compared to the more complicated nonlinear second-order differential equation obtained by applying Newton's second law to a snowplow shock[6]. With our notation, that result is:

$$\xi\frac{d}{d\tau}\left[\left(1-\xi^2\right)\frac{d\xi}{d\tau}\right] = -\frac{4}{9}(\gamma+1)\beta^2(\tau). \tag{7b}$$

Unless $\beta(\xi)$ is known, we must rely on numerical integration for the solution to Eq. (7b). Unlike the snowplow model, Eq. (7a) can be analytically integrated (as long as $\beta(\tau)$ is analytically integrable) to give the dimensionless radius, velocity, and acceleration:

$$\xi = \left[1-\int_0^\tau \beta(t)d\tau\right]^{2/3} \tag{8}$$

$$v \equiv \frac{d\xi}{d\tau} = -\frac{2}{3}\frac{\beta[t(\xi)]}{\xi^{1/2}} = -\frac{2}{3}\frac{\beta(t)}{\left[1-\int_0^\tau \beta(t)d\tau\right]^{1/3}} \tag{9}$$

$$\frac{dv}{d\tau} = v\frac{dv}{d\xi} = \frac{4}{9}\frac{\beta[t(\xi)]}{\xi^{1/2}}\frac{d}{d\xi}\left(\frac{\beta[t(\xi)]}{\xi^{1/2}}\right) = -\frac{2}{9}\frac{\beta^2[t(\xi)]}{\xi^2}\left(1-2\xi\frac{d}{d\xi}\ln\left(\beta[t(\xi)]\right)\right) \tag{10}$$

Significantly, the dimensional drive current appears only in the characteristic time t_0. We apply the implosion model to four different functional forms for the drive current:

$$\beta(\mathrm{t}) = \left(t/t_I\right)^n \tag{11a}$$

$$\beta(\mathrm{t}) = \left(1-t/t_I\right)^n \tag{11b}$$

$$\beta(\mathrm{t}) = \sin\left(\pi/2\cdot t/t_I\right) \tag{11c}$$

$$\beta(\mathrm{t}) = \left[1+\lambda(1-\xi)\right]^{-1}, \tag{11d}$$

which we will refer to, respectively, as rising power law, falling power law, sinusoidal, and a simple circuit model. For both power-law forms, the solutions we will present are

valid for n > -1. In the first three forms, t_I is a characteristic current time. In the simple current model case, we assume that the total inductance per unit length consists of a constant external part and an internal part that is initially zero and increases with convergence ratio: $L_{tot} \sim 1 + \lambda(1 - \xi)$. The parameter λ gives the maximum relative contribution of the internal inductance to the total inductance.

Strictly speaking, the two current forms that start from zero validate our primary model assumptions (small plasma thermal pressure relative to magnetic pressure) for some period of time. However, we anticipate reasonably accurate results as long as the model assumption is met on a timescale that is short compared to the pinch time, Similarly, the assumption of large magnetic pressure can potentially break down part way through the implosion in the decaying-current models, but starting with a sufficiently high current can in many cases ensure that this does not happen before the pinch time.

The snowplow model [Eq. (7b)] is compared to the fast z-pinch model in Fig. 1b. For power-law rising currents with $n \geq 1$, agreement between the two models is remarkably good. As we move to more slowly rising currents, then constant current, then decaying currents, we find that disagreement between the two models becomes large, with the snowplow model predicting an earlier pinch time than the fast z-pinch model. In what follows, we will consider in more detail the fast z-pinch model applied to the various current forms and compare with 1D numerical simulations. For the constant current as well as the decaying current form shown in Fig. 1b, the simulations agree with the fast z-pinch model rather than the snowplow model.

In the case of rising power-law current [Eq. (11a)], we find the plasma implodes according to

$$\xi = \left[1 - \frac{1}{n+1}\tau_I^{-n}\tau^{n+1}\right]^{2/3} = \left[1 - \frac{\tau_I}{n+1}\left(\frac{\tau}{\tau_I}\right)^{n+1}\right]^{2/3}. \tag{12}$$

The pinch time is defined by the time the radius is predicted to go to zero. For the power-law rising current, Eq. (12) gives

$$\tau_p = \left[(n+1)\tau_I^n\right]^{1/(n+1)} = \tau_I\left[(n+1)/\tau_I\right]^{1/(n+1)}. \tag{13}$$

Before calculating the velocity and acceleration (and later the perturbation growth), it is useful to rewrite the current function β in terms of dimensionless radius ξ:

$$\beta(\xi) = \left[(n+1)\tau_I^{-1}\left(1-\xi^{3/2}\right)\right]^{n/(n+1)} \tag{14}$$

Then the velocity and acceleration are given respectively by

$$v = -\frac{2}{3}\frac{1}{\xi^{1/2}}\left[(n+1)\tau_I^{-1}\left(1-\xi^{3/2}\right)\right]^{n/(n+1)} \tag{15}$$

$$\frac{dv}{d\tau} = -\frac{2}{9}\frac{1}{\xi^2}\tau_I^{-2n/(n+1)}\frac{1+n-(1-2n)\xi^{3/2}}{\left[(n+1)\left(1-\xi^{3/2}\right)\right]^{(1-n)/(1+n)}} \tag{16}$$

The radius vs. time predicted by the model for a number of increments is plotted in Fig. (2a), and the velocity and acceleration vs. scale radius are shown in Fig. (2b) for the cases of constant ($n = 0$) and linearly rising ($n = 1$) current. In order to facilitate plotting together results for varying powers n, the characteristic current time t_I is chosen to the keep the implosion time constant and equal to the $n = 0$ value of $t_p = t_0$. That is, we choose $\tau_I = (n+1)^{-1/n}$. The $n = 0$ constant current case is particularly simple, with $\xi = \left[1-\tau\right]^{2/3}$, $\beta(\xi) = 1$, $v = -2/3\cdot\xi^{-1/2}$, and $dv/d\tau = -2/9\cdot\xi^{-2}$.

With falling power-law currents [Eq. (11b)], the dimensionless radius, pinch time, velocity, and acceleration are given by:

$$\xi = \left\{1 - \frac{1}{n+1}\tau_I\left[1 - \left(1 - \frac{\tau}{\tau_I}\right)^{n+1}\right]\right\}^{2/3} \tag{17}$$

$$\tau_p = \tau_I\left\{1 - \left[1 - (n+1)\tau_I^{-1}\right]^{1/(n+1)}\right\} \tag{18}$$

$$v = -\frac{2}{3}\frac{1}{\xi^{1/2}}\left[1 - (n+1)\tau_I^{-1}\left(1 - \xi^{3/2}\right)\right]^{n/(n+1)} \tag{19}$$

$$\frac{dv}{d\tau} = -\frac{2}{9}\frac{1}{\xi^2}\frac{1 - (n+1)\tau_I^{-1} + (1-2n)\tau_I^{-1}\xi^{3/2}}{\left[1 - (n+1)\tau_I^{-1} + (n+1)\tau_I^{-1}\xi^{3/2}\right]^{(1-n)/(1+n)}}. \tag{20}$$

Again, we have made use of the re-expressed current function

$$\beta(\xi) = \left[1 - (n+1)\tau_I^{-1}\left(1 - \xi^{3/2}\right)\right]^{n/(n+1)}. \tag{21}$$

Falling-current results are plotted in Figs. (2c) and (2d). Choosing $n = 0$ of course gives the same constant-current result found in the rising-current form. Here again we have chosen the characteristic current times to give a fixed implosion time. This time the requirement is $\tau_I = n+1$, for which $\xi(t)$ is a power of $\beta(t)$ and $\tau_p = \tau_I$. The parameter choice of $n = ½$ together with $\tau_I = 3/2$, which gives $\beta(t) = \sqrt{1 - 2\tau/3}$, is particularly significant in that it gives constant implosion velocity. In this case post-shock $dv/dt = 0$ as the $1/R^2$ increase in magnetic pressure is exactly balanced by the decrease in drive current. This is apparent in Fig. (2c), and can also be seen by setting the acceleration in Eq. (20) equal to zero.

With the sinusoidal current form [Eq. (11c)], we find

$$\xi = \left\{1 - \frac{2}{\pi}\tau_I\left[1 - \cos\left(\frac{\pi}{2}\frac{\tau}{\tau_I}\right)\right]\right\}^{2/3} \tag{22}$$

$$\tau_p = \frac{2}{\pi}\tau_I\cos^{-1}\left(1 - \frac{\pi}{2}\tau_I^{-1}\right) \tag{23}$$

$$\frac{d\beta}{d\tau} = \frac{\pi}{2}\tau_I^{-1}\left[1 - \frac{\pi}{2}\tau_I^{-1}\left(1-\xi^{3/2}\right)\right] \tag{24}$$

$$\beta(\xi) = \sqrt{\pi\tau_I^{-1}\left(1-\xi^{3/2}\right)\left(1 - \frac{\pi}{4}\tau_I^{-1}\left(1-\xi^{3/2}\right)\right)} \tag{25}$$

$$v = -\frac{2}{3}\sqrt{\frac{\tau_I^{-1}\pi}{\xi}\left(1-\xi^{3/2}\right)\left(1 - \frac{\pi}{4}\tau_I^{-1}\left(1-\xi^{3/2}\right)\right)} \tag{26}$$

$$\frac{dv}{d\tau} = -\frac{2\pi}{9}\frac{\tau_I^{-1}}{\xi^2}\left[1 - \frac{\pi}{4}\tau_I^{-1} + \frac{1}{2}\xi^{3/2} + \frac{\pi}{4}\tau_I^{-1}\xi^3\right] \tag{27}$$

Results of scaled radius vs. time are shown in Figs. (2e), this time together with attendant current profiles. With the sinusoidal form as we have parameterized it, the minimum allowable value of the current time t_I is $\pi/4$ if we require that the current does not change direction before the pinch time. With this maximum value, the current rises to its peak value and then falls back to zero at precisely the implosion time. When the current time is very long compared to the implosion time ($t_I >> t_p$), the plasma sees an essentially linearly-rising current profile.

With the simple circuit model of Eq. (11d), the radius and time are related by

$$\tau = (1+\lambda)(1-\xi^{3/2}) + \tfrac{3}{5}\lambda(1-\xi^{5/2}), \tag{28}$$

which gives the pinch time

$$\tau_p = 1 + \tfrac{8}{5}\lambda \tag{29}$$

The velocity and acceleration are given by

$$v = -\frac{2}{3}\xi^{-1/2}\left[1+\lambda(1-\xi)\right]^{-1} \tag{30}$$

$$\frac{1}{v}\frac{dv}{d\xi} = -\frac{1}{2\xi}\frac{1+\lambda-3\lambda\xi}{1+\lambda-\lambda\xi} \tag{31}$$

As it should, this reduces to the constant current case when $\lambda = 0$. Radius vs. time is plotted in Fig. (2f) for the $\lambda = 0$ constant current case, $\lambda = 1$ for potentially equal contribution of internal and external inductances, and infinite λ for pinch-dominated inductance.

The implosion model is shown in Fig. 3 to compare well up to first bounce with 1D Ares[11] simulations for a variety of current profile forms. Namely, we include constant current [Fig. (3a)], linearly rising current [Fig. (3b)], the $\beta(t) = \sqrt{1 - 2\tau/3}$ falling current case predicted to give a constant implosion velocity [Fig. (3c)], and another falling-current special case that, as will be discussed later, is predicted to be stable according to the instability model. The simulations use hydrogen gas described by tabular equation of state and conductivities, and we specify $P_B(I_0,R_0)/P_{th} \sim 10^4$ based on the dimensional current scale I_0, corresponding to a characteristic Mach number $M(I_0,R_0) \approx 90$. In each case, the red outer curve shows the simulated trajectory of the plasma-vacuum interface. Black lines show simulated Lagrangian trajectories of ten points initially equally spaced in radius in the plasma column. Thus one can follow the propagation of the shock wave as well as the interface motion. Each plot also includes two blues lines generated by the model. The upper blue curve denotes the model-predicted interface trajectory, which overlays the simulation result so well up to first bounce that it is somewhat difficult to discern. The lower blue curve gives a predicted shock trajectory based on mass conservation and assuming constant density across the shocked plasma layer:

$$\xi_s = \xi \sqrt{\frac{1 - \sigma\xi^{-1}}{1 - \sigma\xi}} \tag{32}$$

where the inverse strong shock compression factor $\sigma \equiv (\gamma - 1)/(\gamma + 1)$. Independent of the current profile, this gives $\xi_s = 0$ when $\xi = \sigma$, or $\xi = 1/4$ for $\gamma = 5/3$. The shock trajectory from the simulation is captured reasonably well by this simple model in the constant-current case, but not when the current varies in time. This suggests that gradients in the shocked plasma must be included in order to capture the shock trajectory in general.

In Fig. 4, we plot radial fluid variable profiles in the shocked plasma at $\xi = 0.6$ for the first three cases considered in Fig. 3. The density ratio is $\rho_s^* / \rho_0 \approx 4.2$ at the shock front, corresponding to an effective adiabatic index of 1.6. Density gradients are significant, and non-zero velocity gradients are apparent except in the constant current case. As a measure of the validity of the model assumption Eq. (6), we also define and plot the ratio of ion pressure to fluid velocity squared, scaled to give unity at the shock front:

$$J \equiv (P_i/\rho_0 u^2)[2/(\gamma+1)] \tag{33}$$

According to Eq. (6) and assuming a fully-ionized hydrogen plasma, the quantity J should fall to $(1/\xi)/(1 + Z^*) = 5/6$ at the interface at $\xi = 0.6$. Instead, it rises to about 1.1 in the constant- and falling-current cases, and to 1.3 in the rising-current case. Thus at this radius the model assumption is violated with these current forms at the 30-60% level. However, the fact that the implosion model so effectively describes the plasma-vacuum trajectory in the time-varying-current test cases indicates that the velocity factor in Eq. (6) is an adequate accounting for the gradients. There is no such accounting in the shock trajectory model, which is why it does a poor job in most cases. However, the shock trajectory does not enter directly into the instability model that is the focus of the remainder of this paper, and therefore its inadequacy is not of immediate concern. Its

indirect effect is to limit the time of first bounce that marks the end of the validity of both the implosion model and the instability model to which it serves as input.

III. INSTABILITY MODEL

An RT growth function can be used to characterize instability evolution due to time-dependent acceleration.[12 13] For the z-pinch implosion, we define the RT growth function

$$f(\tau) = \int_0^\tau d\tau \sqrt{-dv/d\tau - \gamma_D}\,, \tag{34}$$

where the first term under the square root is the contributions from interface acceleration in the lab frame, and the second is an effective gravity term present even for constant velocity implosion or hydro-magnetic equilibrium.

For the fast z-pinch, the interface acceleration term from the implosion model is given by Eq. (10). The effective gravity term due to the nonuniform B-field is

$$g_{eff} \equiv \frac{F}{m} = -\frac{P_B A}{\rho^* V^*} = -\frac{2}{R}\frac{P_B}{\rho^*} = -\frac{2}{R}\frac{P_{th}^*}{\rho^*}. \tag{35}$$

The same g_{eff} comes from considering $E \times B$ drifts due to field gradient and curvature. In our dimensionless units and assuming that density varies across the shocked plasma layer only due to cylindrical convergence, we have

$$\gamma_D \equiv g_{eff} t_0^2 / R_0 = -\frac{4(\gamma-1)}{9}\frac{\beta^2}{\xi^2} = -(\gamma-1)\frac{v^2}{\xi}. \tag{36}$$

This effective gravity term is always significant compared to the interface acceleration term. Inserting both terms into Eq. (34) for the growth function, we find

$$f(\xi) = \int_{\xi}^{1} d\xi \sqrt{-\frac{1}{v}\frac{dv}{d\xi} - \frac{\gamma_D}{v^2}} = \int_{\xi}^{1} \frac{d\xi}{\sqrt{2\xi}} \sqrt{\left(1 - 2\xi \frac{d}{d\xi} \ln(\beta[t(\xi)])\right) + [2(\gamma - 1)]} \quad (37a)$$

$$= \sqrt{\gamma - \tfrac{1}{2}} \int_{\xi}^{1} \frac{d\xi}{\sqrt{\xi}} \sqrt{1 - \frac{1}{\gamma - \tfrac{1}{2}} \xi \frac{d}{d\xi} \ln(\beta[t(\xi)])} \quad (37b)$$

The utility of considering the RT growth function is that it can be used to represent all of the time dependence in models of nonlinear single mode and "turbulent" multimode models based on buoyancy-drag or self-similarity. In addition, for accelerations that are constant in time, the linear growth[2] is exponential in *f*:

$$a(t)/a_0 = \exp\{\sqrt{kR_0} f(t)\}. \quad (38)$$

Based on a terminal-velocity buoyancy-drag model,[7,10] nonlinear single-mode growth is linear in *f*:

$$h_{nl}(t)/R_0 = \sqrt{C_D^{-1} \lambda / R_0} f(t), \quad (39)$$

where the drag coefficient for bubbles is given by $C_D = \{3\pi, \beta_1\}_{2D,3D}$ and β_1 is the first root of the zero-order Bessel function.[7,14] Based on self-similar growth[15] or bubble-merger[16,17] models that describe the inverse cascade from smaller to larger perturbation scales, multimode turbulent mix widths are given by:[18,19]

$$h_{\alpha}(t)/R_0 = \left[\sqrt{h_0/R_0} + \sqrt{\alpha} f(t)\right]^2 = h_{nl}/R_0 + \alpha f^2(t), \quad (40)$$

where the parameter $\alpha_b \approx 0.06$ for bubbles in classical RT and $\alpha_s \rightarrow \frac{1}{2}$ as $A \rightarrow 1$.[20] Such models can give asymptotic mix widths that are quadratic in *f* and independent of the initial conditions (perturbation amplitude and wavelength) once $\sqrt{\alpha} f(t) >> \sqrt{h_0/R_0}$. In order for this loss of memory of initial conditions to occur before the bubble tips reach the axis [$h_{\alpha}(t)/R = 1$], the model requires $\sqrt{h_0/R_0} << \sqrt{\xi_{min}}/2$, or $h_0/R_0 < \xi_{min}/400$.

Note that this result depends on the model parameter α only implicitly through the minimum radius $\xi_{\min}$.

If the total acceleration in Eq. (34) is constant in time and we allow for Atwood number less than unity, then we recover the classical asymptotic result[16] $h(t) = \alpha A g_{tot} t^2$. Neglecting the effective gravity term and driving the instability growth with the interface acceleration term only, we find that the asymptotic turbulent mix widths scale with the distance traveled by the interface $\zeta(t) \equiv 2A\int\int dtdt' g(t')/R_0 = 2A(1-\xi^{-1})$ as long as the interface acceleration is a power law in time $g \sim t^m$ with $m > -1$. Since this is not true in general, and in any case the effective gravity term is significant relative to the interface acceleration term, instability growth in a z-pinch is not proportional to the distance traveled by the interface.

For power-law rising currents, the implosion model gives the RT growth function

$$f(\xi) = \sqrt{\gamma - \tfrac{1}{2}}\int_{\xi}^{1} \frac{d\xi}{\sqrt{\xi}} \sqrt{1 + \frac{1}{2\gamma - 1}\frac{3n}{n+1}\frac{\xi^{3/2}}{1-\xi^{3/2}}}\,, \tag{41}$$

while for falling power-law currents the result is

$$f(\xi) = \sqrt{\gamma - \tfrac{1}{2}}\int_{\xi}^{1} \frac{d\xi}{\sqrt{\xi}} \sqrt{1 + \frac{1}{2\gamma - 1}\frac{3n}{n+1}\frac{\xi^{3/2}}{1-\xi^{3/2} - \tau_f/(n+1)}}\,. \tag{42}$$

Both give $f(\xi) = 2\sqrt{\gamma - \tfrac{1}{2}}\left(1 - \xi^{1/2}\right)$ for constant current ($n = 0$). With the constant implosion velocity falling current case of $n = 1/2$, $t_f = 3t_0/2$, $\beta(t) = \left(1 - 3\tau/2\right)^{1/2}$, Eq. (42) gives the RT growth function $f(\xi) = 2\sqrt{\gamma - 1}\left(1 - \xi^{1/2}\right)$, which is less that the constant-current growth by a constant factor $\sqrt{(\gamma - 1)/(\gamma - 1/2)}$. Without the effective gravity term, the model would in this case predict no instability (i.e. $f = 0$) for this case. Equation

(37b) does, however, vanish in the event that $\beta(\xi) = \xi^{\gamma-1/2}$. This special case is analogous to conducting a gravitational RT experiment inside a free-falling laboratory, and corresponds to a power-law falling current with $n = (\gamma - 1/2)/(2-\gamma)$, $\tau_I = \tau_p = 1.5/(2-\gamma)$. For $\gamma_{eff} = 1.6$ this gives or $n = 2.75$, $\tau_I = 3.75$. As shown in Fig. 3d, the 1D pinch dynamics are captured well by the implosion model up to first bounce, but we find a disappointing $CR_{max} = 2.2$ due to the rapidly falling current. This minimum radius is reached at $\tau_I \approx 1.2 \approx \tau_p/3$. Even in the absence of instabilities, such rapidly falling currents do not deliver high plasma compression.

The effect of the two terms in Eq. (34) on the linear instability growth is explored in Fig. 5 by comparing the model predictions to a 2D Ares simulation of a single mode perturbation, driven by a constant current source, with and without interface acceleration. Equation (38) is only valid for constant acceleration, so we can only apply it as an approximation when the interface convergence is very small. In Fig. 5a, we initialize the problem in hydro-magnetic equilibrium so that $dv/dt = 0$ and only the effective gravity term contributes. While the perturbation remains linear, the model does a reasonable job of describing the instability growth. In Fig. 5b, the condition for a fast z-pinch is satisfied. During the linear phase, including either just the interface acceleration term or the effective gravity term results in an under-prediction of the growth. When both terms are included, the linear growth is well described by the model. The effective gravity term gives the larger contribution, but neither is negligible.

As long as the fast-implosion model is valid, the instability growth vs radius is never affected by the dimensional drive current. For power-law rising currents, Eq. (41) suggests that instability growth is also not affected by the characteristic current time t_I -

only by its functional form. However, the characteristic current time does affect the growth with falling currents. The inevitability of this statement is easily seen by considering that, as the current decay time becomes long compared to the implosion time, the system behavior must approach the constant-current case. Conversely, in the $t_I << t_0$ limit, the falling-current growth as a function of radius is equal to the t^n growth for the same n. Of course if the current decay is too rapid then the implosion will not reach a minimum radius as small as in the rising-current case, so the instability growth actually realized during the pinch will be less.

Turbulent mix widths predicted by the model for rising and falling power-law currents are shown in Fig. 6a. The perturbations amplitudes are normalized to the instantaneous radius of the unperturbed interface, and are plotted against scaled radius. For reasons that will be discussed later, we use $\alpha = 0.108$ instead of the $\alpha \approx 0.06$ typical of classical RT. Constant current produces more mix than falling currents, and rising currents produce more mix than constant or falling currents.

With constant current, we can write simple analytic expressions for the predicted instability growth. The nonlinear single-mode growth for 2D bubbles driven by a constant current is

$$h_{nl}/R = 2\sqrt{(\gamma - \tfrac{1}{2})/(3\pi)\lambda/R_0}\left(1-\xi^{1/2}\right)/\xi . \qquad (43)$$

We define the maximum convergence ratio for an axially-coherent pinch (CR_{max}) limited by instability growth as the CR based on the unperturbed interface position for which instability bubbles are predicted to reach the origin. For a nonlinear single-mode perturbation, we find $h_{nl}/R = 1$ at

$$CR_{max} = 1/\xi_{min}$$
$$= \left[4(\gamma - \tfrac{1}{2})/(3\pi)\lambda/R_0 + 2\sqrt{(\gamma - \tfrac{1}{2})/(3\pi)\lambda/R_0}\left(1 - \sqrt{1 + 2\sqrt{(\gamma - \tfrac{1}{2})/(3\pi)\lambda/R_0}/4}\right)\right]^{-1} \quad (44)$$

Assuming infinitely small initial amplitudes with proportional wavelengths, turbulent mix widths are given by

$$h_\alpha/R = 4(\gamma - \tfrac{1}{2})\alpha\left(1/\xi^{1/2} - 1\right)^2. \quad (45)$$

The maximum *CR* for an axially coherent pinch limited by multimode perturbation growth is therefore

$$CR_{max} = 1/\xi_{min} = \left[1 + 1/\left(2\sqrt{(\gamma - \tfrac{1}{2})\alpha}\right)\right]^2 \quad (46)$$

This gives $CR_{max} \approx 8.4$ for $\alpha = 0.060$ and $CR_{max} \approx 5.8$ for $\alpha = 0.108$.

For varying *n*, the CR_{max} predicted by the asymptotic turbulent mix model is shown in Fig. 7. Again, we see that constant current produces more mix than falling currents, and rising currents produce more mix than constant or falling currents. For power-law rising currents at high *n*, CR_{max} asymptotes to a minimum value of about three.

We previously noted that for power-law falling currents the instability growth and even the nature of the implosion depend on the current decay time. Yet in Fig. 7a we gave only the results as a function of *n* for the case of τ_I equal to the critical value $\tau_{I,crit} = n + 1$ at which $\xi(t)$ is a power of $\beta(t)$ and $\tau_p = \tau_I$. In Fig. 9a, we show the pinch radius vs. time predicted by the model for a fixed $n = 1/2$ and four different values of τ_I. At infinite τ_I, the result is identical to the constant-current case. Below the critical scaled rise time $\tau_{I,crit} = 3/2$, the plasma does not fully implode. Consequently, for $\tau_I < \tau_{I,crit}$ we find that

CR_{max} is limited by the 1D implosion rather than by the instability. At $\tau_{l,crit}$, CR_{max} is maximized, and above $\tau_{l,crit}$ it approaches the constant current value as expected.

For the sinusoidal current form, the RT growth function is

$$f(\xi) = \sqrt{\gamma - \tfrac{1}{2}} \int_{\xi}^{1} \frac{d\xi}{\sqrt{\xi}} \sqrt{1 + \frac{1}{2\gamma - 1} \frac{3}{2} \frac{\xi^{3/2}}{1 - \xi^{3/2}} \frac{1 - (\pi/2\tau_I)(1 - \xi^{3/2})}{1 - (\pi/4\tau_I)(1 - \xi^{3/2})}}, \tag{47}$$

and the predicted turbulent mix with is shown in Fig. 6b for three different values of τ_I. When $t_I >> t_0$, the current rise is essentially linear in time and the growth is the same as predicted by Eq. (41) with $n = 1$ independent of the current rise time. Reducing t_I/t_0 results in reduced instability growth, with the smallest growth attained in the case that the current climbs to its maximum and then returns to zero just as the pinch radius goes to zero ($\tau_I = \pi/4 = t_p/2$). The limiting convergence ratio is therefore maximized (CR_{max} = 4.7) for $t_I = \pi/4$ (See Fig. 7b). For $t_I < t_p$, CR_{max} is strongly dependent on t_I, while for $t_I > t_p$ it asymptotes to the $n = 1$ rising current value of 3.6.

With the simple circuit model [Eq. (11d)], the RT growth function is

$$f(\xi) = \int_{\xi}^{1} \frac{d\xi}{\sqrt{2\xi}} \sqrt{2(\gamma - 1) + \frac{1 + \lambda - 3\lambda\xi}{1 + \lambda - \lambda\xi}}, \tag{48}$$

which again agrees with the constant current case in the $\lambda \rightarrow 0$ limit. The limiting CR_{max} is plotted in Fig. 7c as a function of λ. As λ increases from zero, CR_{max} climbs from the constant-current value of 5.8 and approaches an asymptotic value of 14.5 as λ approaches infinity. This is qualitatively consistent with the prediction based on power-law currents that a more rapidly decaying current yields less instability growth as a function of radius.

IV. NUMERICAL SIMULATIONS

High-resolution 2D numerical simulations illustrate the nonlinear instability growth and facilitate calibration of the instability model. The numerical system is the same as that described earlier for the 1D calculations, namely a hydrogen plasma driven by a magnetic pressure (based on the characteristic dimensional current) that is of order 10^4 times the initial thermal pressure. In the 2D simulations, perturbations are imposed on the outer surface of the plasma. In all cases, the initial perturbation is a single mode with $ka = 0.45$, $\lambda_0/R_0 = 0.025$, and with 10 wavelengths in the domain. The initial mode in these calculations is only moderately resolved with $\lambda_0/\Delta z = 10$, where Δz is the axial grid resolution.

Density plots from simulations with three different current profiles are shown in Fig. 9 at various radii. Qualitatively, the results agree in several respects with the nonlinear instability models as applied to the fast z-pinch model. All three show development of significant nonlinear growth initiated by the seed mode prior to first bounce. Constant current produces slightly more growth than the $n = 1/2$ falling-current case that gives constant implosion velocity in 1D. The linearly rising current produces much more growth than the constant- and falling-current cases and the difference is apparent almost immediately. When the current is high from time zero, the outer plasma is imparted a post-shock inward velocity before instability growth is initiated. Consequently, all plasma behind the shock is seen to move inward, including the developing instability spikes. In the rising-current case, on the other hand, there is a very brief initial period of subsonic implosion. As the instability growth is also initiated during

this period, some plasma is left behind at the initial cylinder radius, resulting in spike lengths equal to the distance traveled by the interface.

In all three cases, an inverse cascade to larger scales is evident within about CR = 2, justifying application of the multimode instability growth model. The bubble amplitude growth observed in the simulations is compared with four different sets of model parameters in Fig. 10. In Fig. 10a, we use $\alpha = 0.06$ typical of classical multimode RT and neglect the initial amplitude in Eq. (40). This results in significantly less growth than observed in the simulations. In Fig. 10b, we again neglect the initial amplitude but increase α to a value of 0.210, or 3.5 times the classical value, in order to bring the model in line with the simulations. In Fig. 10c, we return to $\alpha = 0.06$ but now include the initial amplitude, yielding growth that is closer to the simulations but still low. Comparison of Figs. 10a and 10c suggests that during the implosion the system does not have time to enter the asymptotic regime independent of the initial conditions. According to the model, doing so with $CR_{max} = 4$ would require an initial amplitude shorter than about 1/1600 the initial gas radius – much smaller than the $h_0/R_0 \approx 1/559$ in the simulation. At higher CR_{max}, the requirement is stricter still.

Finally, in Fig. 10d we include the initial amplitude in the model and increase α to a value of 0.108, or 1.8 times the typical classical value, in order to achieve the best overall agreement with the simulations. In its present form, the model suffers from two main limitations that should cause it to underpredict the bubble acceleration, and consequently the instability growth. First of all, instability growth produces trailing mass and therefore reduces the plasma density at the unperturbed interface position. Second, the model uses the magnetic pressure at the unperturbed interface position rather than at

the bubble tip, which is at smaller radius. Consequently, it should be no surprise that for best fit to data the model requires α higher than the classical RT value.

Similarly, we might expect the same model limitations to invalidate the prediction that the $\beta(\tau) = \left[1 - 2(2-\gamma)\tau/3\right]^{(\gamma-1/2)/(2-\gamma)}$ case is stable. Figure 11 includes a density plot from a relevant 2D simulation at $\xi = 0.48$, which is near the $\xi_{min} = 0.45$. The instability growth is indeed non-zero, but is greatly reduced relative to all three cases presented in Figs. 9-10. As noted previously, even in the absence of instabilities such rapidly falling currents do not provide high plasma compression.

V. CONCLUSIONS

The implosion dynamics of a high-field fast z-pinch are described effectively by a very simple strong shock model that can be solved analytically for a variety of current forms. The model is valid up to first bounce as long as the magnetic pressure remains large compared to the initial plasma pressure. For constant drive current, mass conservation assuming uniform gradients in the shocked plasma captures the shock trajectory reasonably well.

Rayleigh-Taylor growth at the plasma-field interface is driven by interface acceleration as well as the effective gravity present in the equilibrium configuration. Growth function analysis provides predictions for nonlinear single mode and multimode "turbulent" Rayleigh-Taylor growth and places limits on the maximum convergence possible for an axially coherent pinch. Rising currents are predicted to produce faster

growth, as a function of radius, than are constant currents, and decaying currents yield less growth than constant currents.

Linear-phase simulations compare well with the model in both equilibrium and non-equilibrium systems. Nonlinear-phase simulations exhibit growth that agrees qualitatively with the model predictions. Quantitative agreement requires a turbulent-mix growth parameter α that is nearly twice as high as the typical for classical RT

VI. ACKNOWLEDGEMENTS

In preparing this manuscript, I was greatly benefited by discussions with and input from Jim Hammer, Omar Hurricane, and Mark Adams. This work was performed under the auspices of the U.S. Department of Energy by Lawrence Livermore National Laboratory under Contract DE-AC52-07NA27344.

VII. REFERENCES

[1]J. W. S. Rayleigh, *Scientific Papers* (Cambridge University Press, Cambridge, 1899).

[2]G. I. Taylor, Proc. R. Soc. London, Ser A **201**, 192 (1950).

[3]M. Kruskal and M. Schwarzschild, proc. Roy. Soc. London, Ser. A **223**, 348 (1954).

[4]V. D. Shafranov, Atomnaya Energiya **5**, 38 (1956).

[5]M. N. Rosenbluth and C. L. Longmire, Ann. Phys. **1**, 120 (1957).

[6]O. A. Anderson, W. R. Baker, S. A. Colgate, J. I. Ise,Jr., and R. V. Pyle, Phys. Rev. **109**, 612 (1958).

[7]R. M. Davies and G. I. Taylor, Proc. R. Soc. London, Ser. A **200**, 375 (1950).

[8]J. C. V. Hanson, P. A. Rosen, T. J. Goldsack, *et al.*, Laser Part. Beams **8**, 51 (1990).

[9]G. Dimonte and M. Schneider, Phys. Rev. E **54**, 3740 (1996).

[10]D. Oron, L. Arazi, D. Kartoon, *et al.*, Phys. Plasmas **8**, 2883 (2001).

[11]G. Bazan, Proceedings from the 2nd International Workshop on Laboratory Astrophysics with Intense Lasers, UCRL-ID-131978, ed. B. A. Remington, 42 (Lawrence Livermore National Laboratory, Livermore, CA 1998).

[12]A. R. Miles, Phys. Plasmas **11**, 5140 (2004).

[13]A. R. Miles, Astrophys. J., submitted (2008).

[14]D. Layzer, Astrophys. J. **122**, 1 (1955).

[15]D. L. Youngs, Physica D **12**, 32 (1984).

[16]K. I. Sharp, Physica D **12**, 3 (1984).

[17]J. Glimm and X. L. Li, Phys. Fluids **31**, 2077 (1988).

[18]K. I. Read, Physica D *12*, 45 (1984).

[19]G. Dimonte and M. Schneider, Phys. Fluids **12**, 304 (2000).

[20]G. Dimonte, D. L. Youngs, A. Dimits, S. Weber, M. Marinak, *et al.*, Phys. Fluids **16**, 1668 (2004).

Fig. 1. (a) Z-pinch geometry. A time-dependent electric current travels down the outside of an imploding plasma cylinder with initial radius R_0. (b) Pinch radius vs. time for drive current that is linear in time (blue), constant (black), and falling to zero like the square root of the time to pinch (red). Solid and dashed lines denote the fast z-pinch model, while dotted lines give the standard snowplow model prediction.

Fig. 2. Fast z-pinch implosion model predictions for (a) power-law rising current radius vs time, (b) power-law rising current velocity and acceleration vs radius, (c) power-law falling current radius vs time, (d) power-law falling current velocity and acceleration vs radius, (e) sinusoidal-current radius vs time and drive current function, and (f) circuit model radius vs time.

Fig. 3. Comparison of fast z-pinch implosion model with 1D Ares simulations for (a) constant current, (b) linearly rising current, (c) $n = 1/2$ power-law falling current, and (d) $n = 2.75$ power-law falling current. Black lines denote simulation radius-vs-time trajectories of initially equally spaced lagrangian fluid elements. Red lines show simulation plasma-vacuum interface trajectories. Upper blue lines show plasma-vacuum interface predicted by the model, and lower blue lines give the predicted shock trajectories assuming mass conservation and no gradients in the shocked plasma.

Fig. 4. Shocked-plasma radial profiles from 1D Ares simulations for (a) constant current, (b) linearly rising current, and (c) $n = 1/2$ power-law falling current. Densities are

normalized to the preshock value and scaled by a factor of ten, velocities are scaled by twice their peak value, and $J \equiv (P_i/\rho_0 u^2)[2/(\gamma+1)]$ is related to the model assumption in Eq. (6) as discussed in the text.

Fig. 5. Linear-phase perturbation growth agrees well with the model: (a) Hydro-magnetic equilibrium initial configuration with contribution from effective gravity term only. (b) Fast pinch with significant contributions from both interface acceleration term and effective gravity term.

Fig. 6. Turbulent mix model with $\alpha = 0.108$ applied to fast z-pinch for (a) Power-law currents and (b) sinusoidal currents.

Fig. 7. Turbulent mix model ($\alpha = 0.108$) maximum convergence ratio for axially coherent fast z-pinch with (a) power-law currents, (b) sinusoidal currents, and (c) circuit model.

Fig. 8. With falling currents, the characteristic current decay time affects the nature of the implosion as well as the instability growth vs radius. (a) Radius vs time for several different decay times, all with $n = 1/2$. Below the critical decay time, the plasma fails to implode completely. With $n = 1/2$, the implosion velocity is constant at a critical decay time. (b) CR_{max} vs current decay time with $\alpha = 0.108$. Perturbation growth is minimized at the critical decay time. Below the critical decay time, CR_{max} is limited by the 1D implosion dynamics rather than the instability.

Fig. 9. Density plots from high-resolution numerical simulations illustrate the nonlinear instability growth and provide mix mode calibration. Within each panel, the left-most image is from a simulation driven with an $n = 1/2$ falling current at the critical current decay time, the middle image is constant current, and the right-most image is linearly rising current.

Fig. 10. Comparison of nonlinear multimode model and 2D numerical simulations for constant, linearly rising, and $n = 1/2$ falling current with the critical current decay time. Lines denote model results, and symbols represent simulation results. (a) $\alpha = 0.060$ and initial amplitude neglected, (b) $\alpha = 0.210$ with initial amplitude neglected, (c) $\alpha = 0.060$ and initial amplitude included, (d) $\alpha = 0.108$ with initial amplitude included.

Fig. 11. Density plots from high-resolution numerical simulations near minimum radius for the $n = 2.75$, $\tau_I = 3.75$ falling current case. This special case, predicted by the model to be stable, is the leftmost image. To its right are the $n = 1/2$ falling current case, constant current, and linearly rising current.

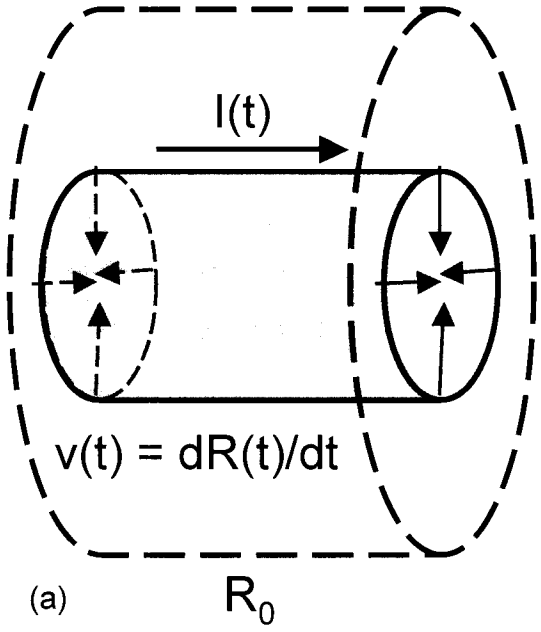
I(t)
v(t) = dR(t)/dt
(a)
R_0

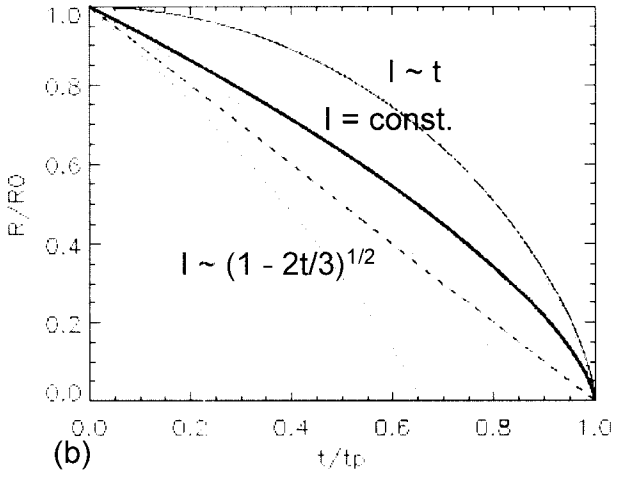
1.0
0.8
0.6
0.4
0.2
0.0
R/R0
I ~ t
I = const.
I ~ (1 - 2t/3)^1/2
0.0
0.2
0.4
0.6
0.8
1.0
t/tp
(b)

Fig. 1

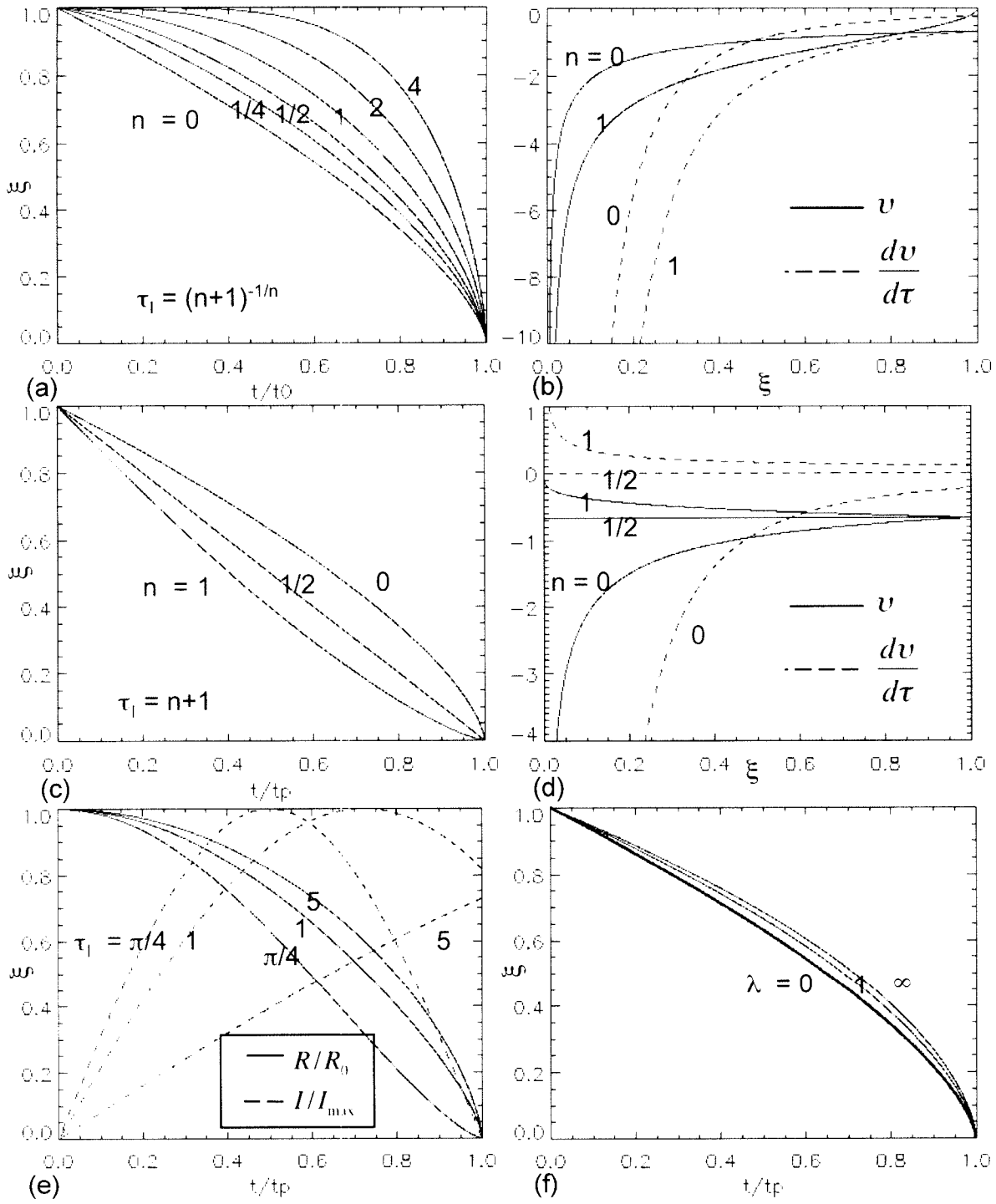
(a)
n = 0
1/4 1/2 1 2 4
$\tau_1 = (n+1)^{-1/n}$
ξ
t/t0
(b)
n = 0
1
0
1
v
$\frac{dv}{d\tau}$
ξ
(c)
n = 1
1/2
0
τ_1 = n+1
ξ
t/tp
(d)
1
1/2
1
1/2
n = 0
0
v
$\frac{dv}{d\tau}$
ξ
(e)
$\tau_1 = \pi/4$ 1
5
1
π/4
5
R/R_0
I/I_{max}
ξ
t/tp
(f)
λ = 0
1
∞
ξ
t/tp

Fig. 2

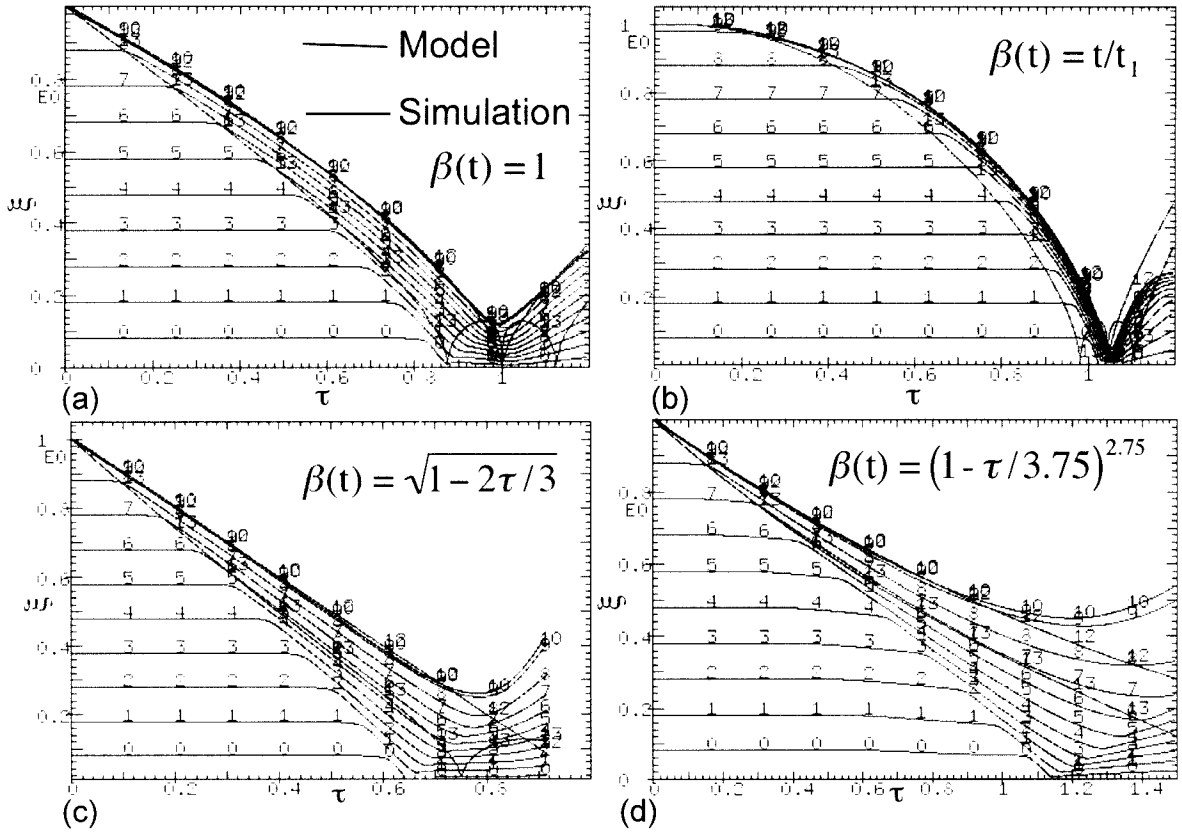
Model
Simulation
$\beta(t) = 1$
(a)
$\beta(t) = t/t_1$
(b)
$\beta(t) = \sqrt{1 - 2\tau/3}$
(c)
$\beta(t) = (1 - \tau/3.75)^{2.75}$
(d)
EO
ω
τ

Fig. 3

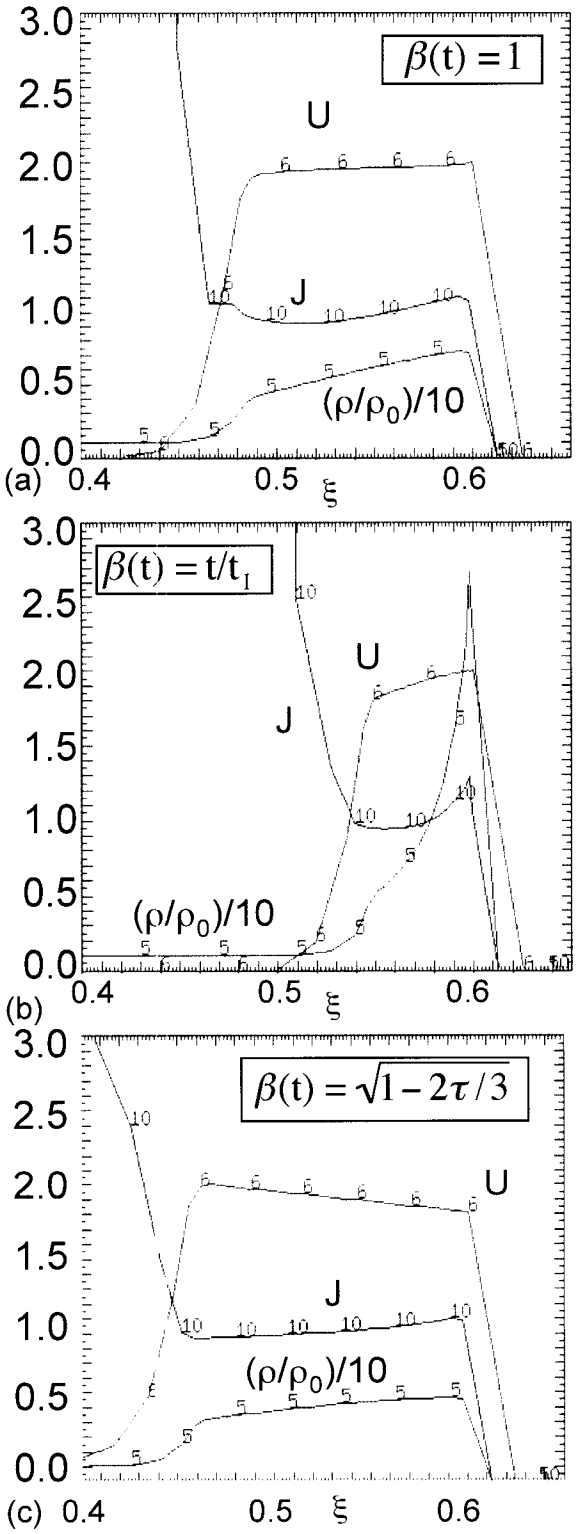
3.0
2.5
2.0
1.5
1.0
0.5
0.0
β(t) = 1
U
J
(ρ/ρ0)/10
(a)
0.4
0.5
ξ
0.6
β(t) = t/tI
U
J
(ρ/ρ0)/10
(b)
0.4
0.5
ξ
0.6
β(t) = √(1 − 2τ/3)
U
J
(ρ/ρ0)/10
(c)
0.4
0.5
ξ
0.6

Fig. 4

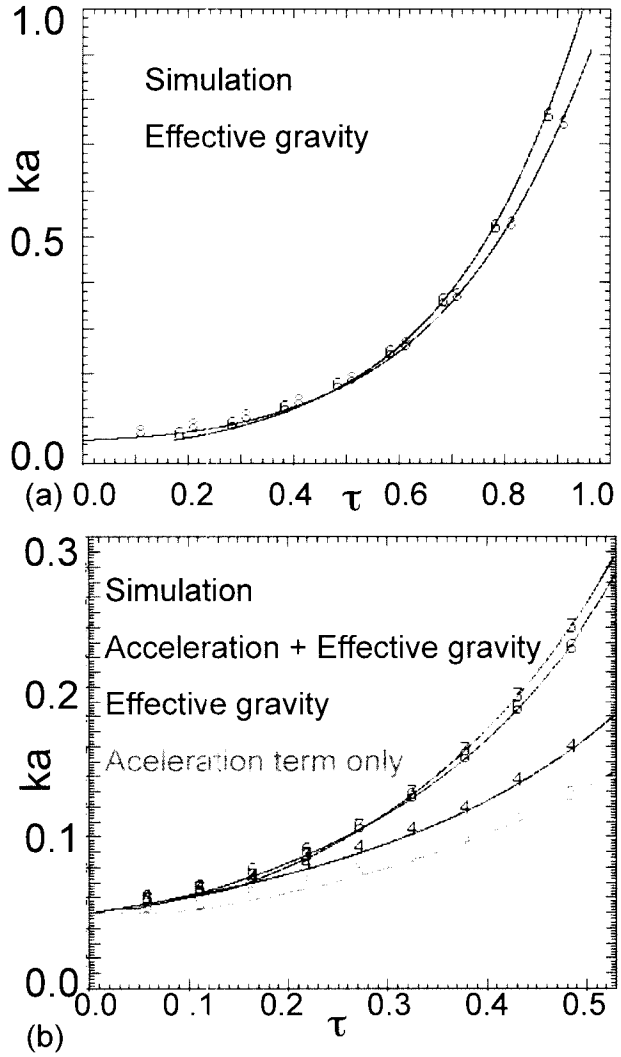
1.0
0.5
0.0
ka
Simulation
Effective gravity
(a) 0.0
0.2
0.4
τ
0.6
0.8
1.0
0.3
0.2
0.1
0.0
ka
Simulation
Acceleration + Effective gravity
Effective gravity
Aceleration term only
0.0
0.1
0.2
0.3
0.4
0.5
τ
(b)

Fig. 5

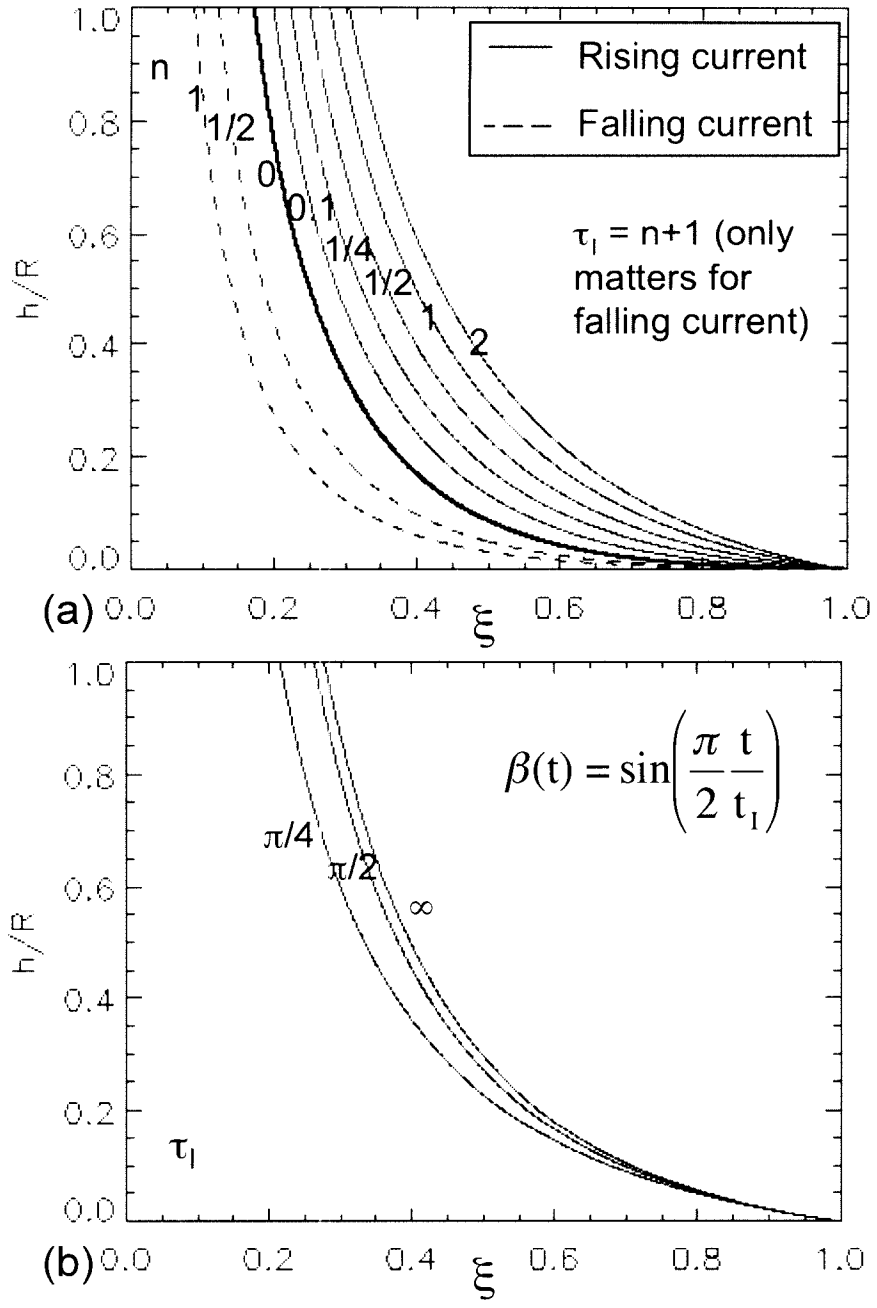
Rising current
Falling current
n
1
1/2
0
0.1
1/4
1/2
1
2
τ_I = n+1 (only matters for falling current)
h/R
ξ
(a)
$\beta(t) = \sin\left(\frac{\pi}{2}\frac{t}{t_I}\right)$
π/4
π/2
∞
τ_I
(b)

Fig. 6

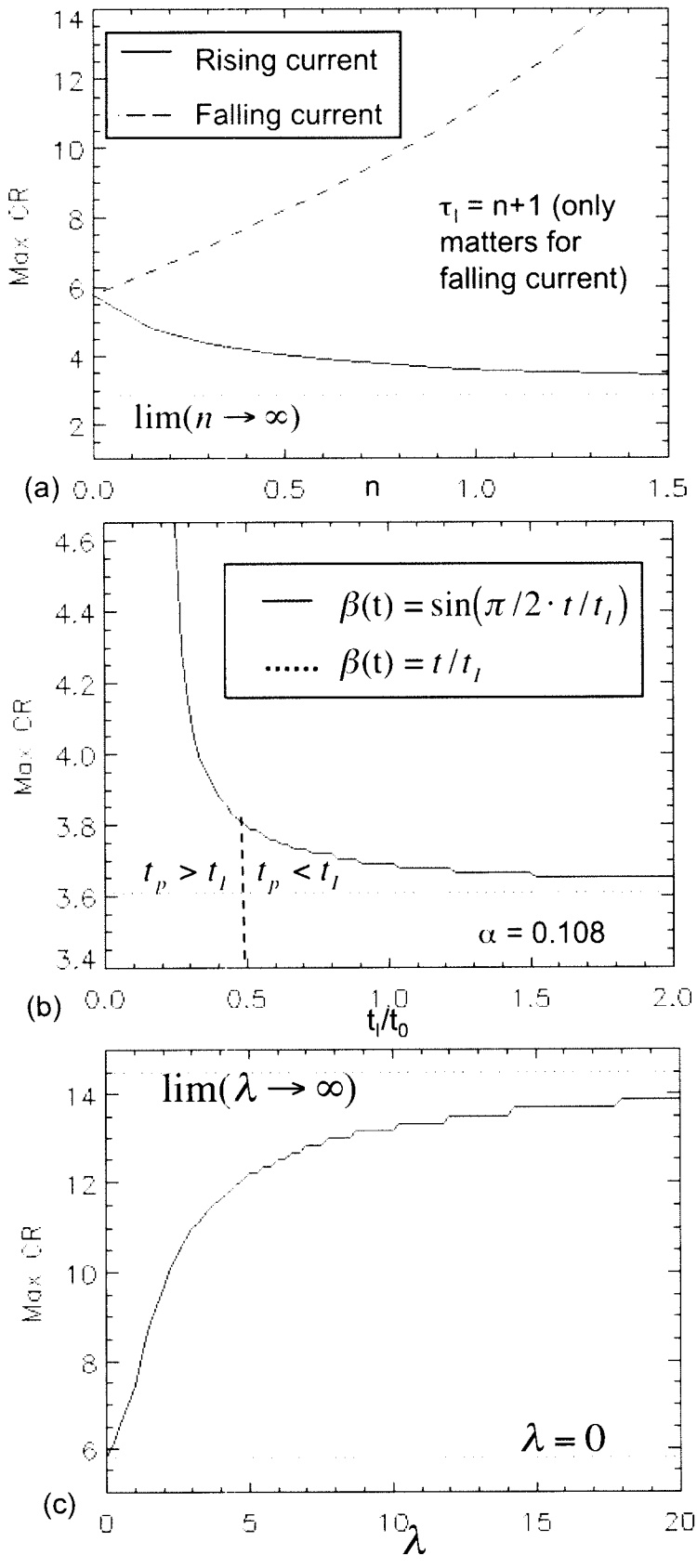
Rising current
Falling current
τ_l = n+1 (only matters for falling current)
$\lim(n \to \infty)$
Max CR
n
(a)
$\beta(t) = \sin(\pi/2 \cdot t/t_l)$
$\beta(t) = t/t_l$
$t_p > t_l$
$t_p < t_l$
α = 0.108
t_l/t_0
(b)
$\lim(\lambda \to \infty)$
$\lambda = 0$
λ
(c)

Fig. 7

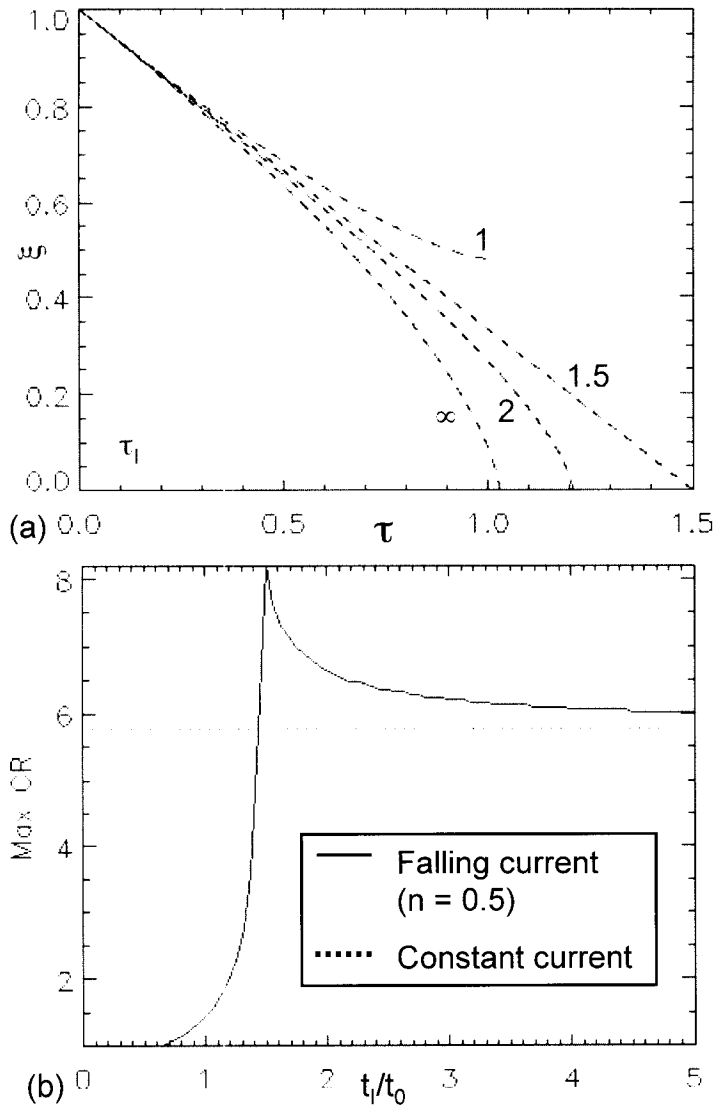
1.0
0.8
0.6
ξ
0.4
0.2
0.0
τ_I
1
1.5
2
∞
(a) 0.0
0.5
τ
1.0
1.5
8
6
4
2
Max CR
Falling current
(n = 0.5)
Constant current
(b) 0
1
2
t_I/t_0
3
4
5

Fig. 8

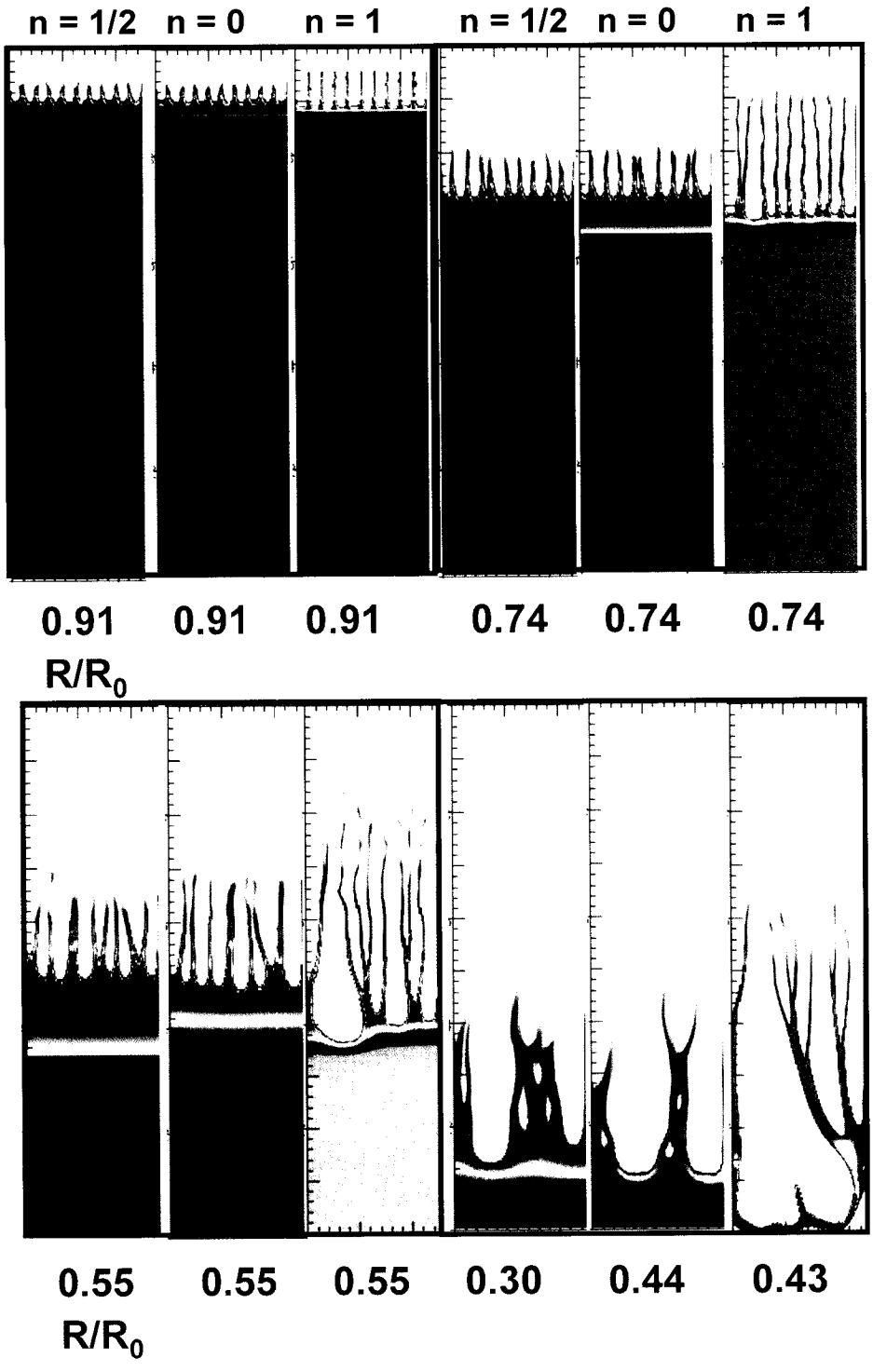
n = 1/2
n = 0
n = 1
n = 1/2
n = 0
n = 1
0.91
0.91
0.91
0.74
0.74
0.74
R/R0
0.55
0.55
0.55
0.30
0.44
0.43
R/R0

Fig. 9

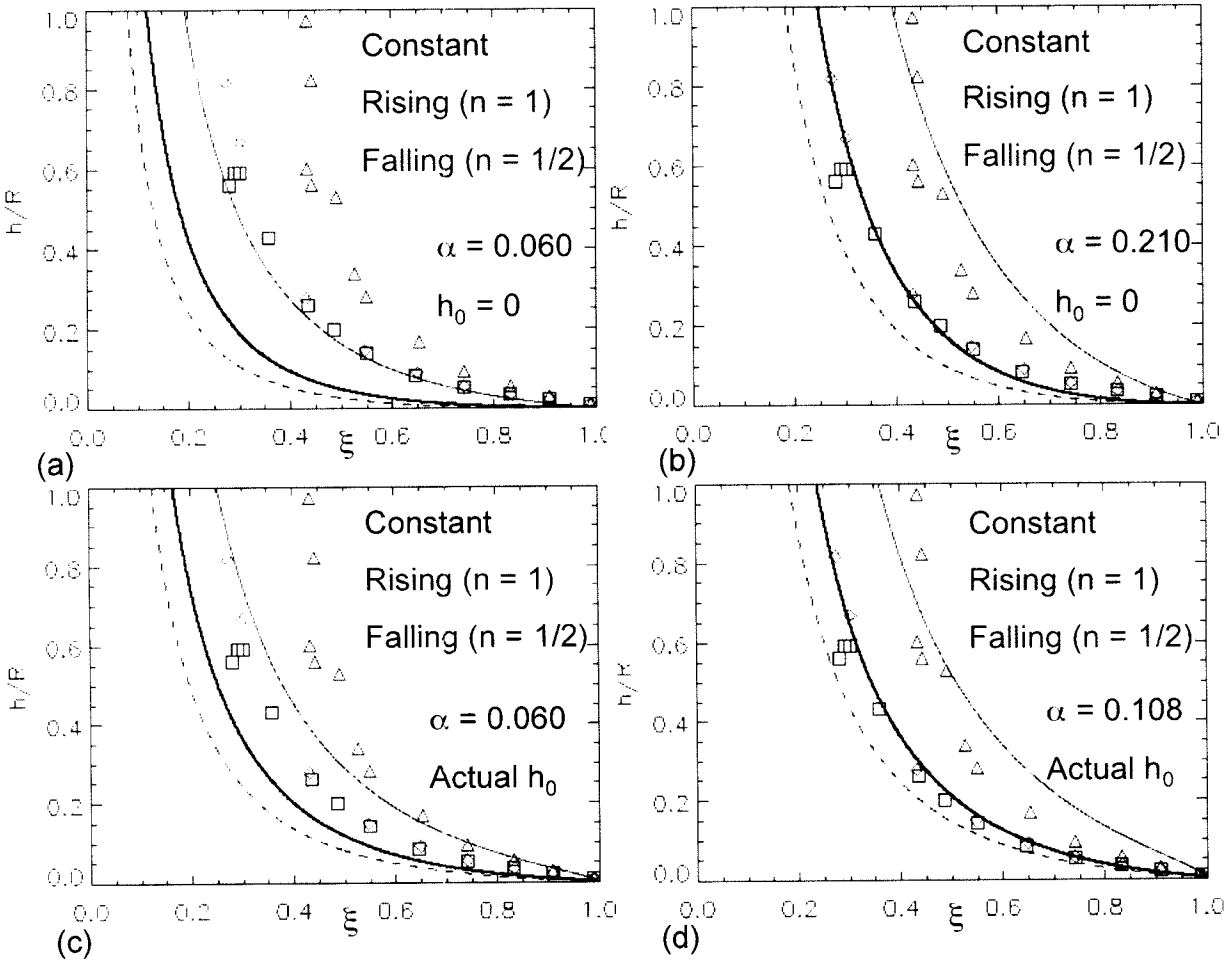
Constant
Rising (n = 1)
Falling (n = 1/2)
α = 0.060
h0 = 0
(a)
Constant
Rising (n = 1)
Falling (n = 1/2)
α = 0.210
h0 = 0
(b)
Constant
Rising (n = 1)
Falling (n = 1/2)
α = 0.060
Actual h0
(c)
Constant
Rising (n = 1)
Falling (n = 1/2)
α = 0.108
Actual h0
(d)
h/R
ξ
0.0
0.2
0.4
0.6
0.8
1.0

Fig. 10

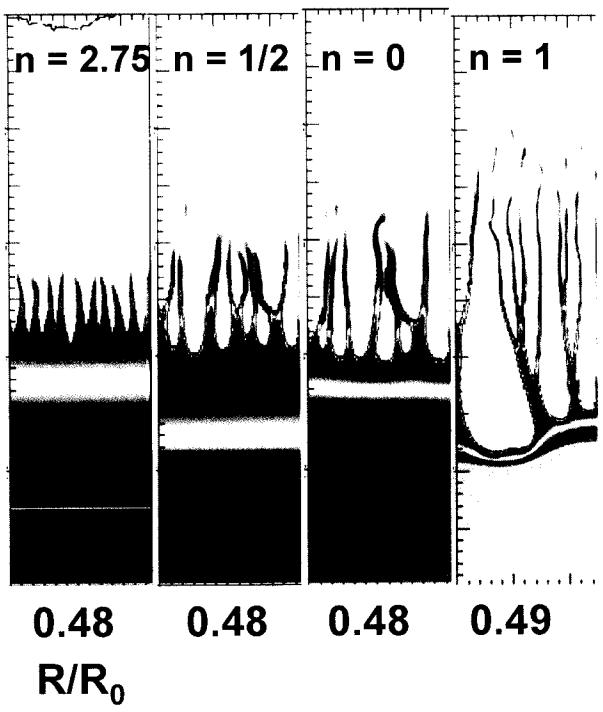

Fig. 11